What triggers failure in frictional granular assemblies?

Philipp R. Welker

Institut für Computerphysik, Universität Stuttgart, 70569 Stuttgart, Germany

Sean C. McNamara

Institut de Physique de Rennes, UMR UR1-CNRS 6251, Université de Rennes 1,
Bât. 11A, Campus de Beaulieu, 35042 Rennes Cedex, France

We examine numerically the yielding or failure of small granular packings subjected to an increasing deviatoric stress. As the load increases, the packing softens and the number of sliding contacts rises. When the packing fails, the kinetic energy starts to rise exponentially in time. It is always possible to identify a contact status change that triggers the collapse of the packing. Furthermore, by use of the stiffness matrix, we show that this change often causes a mechanical instability or a motion with neutral stability. In some cases, the status change provokes an oscillation and a second status change following shortly thereafter introduces an instability. Failure can also be considered from the perspective of energy flux: before failure, the energy injected by the load is stored as potential energy in the contacts. When this is no longer possible, failure occurs and the injected energy is converted to kinetic energy. However, the force disequilibrium then soon becomes the dominant energy source.

PACS number(s): 83.80.Fg, 81.05.Rm, 81.70.Bt, 81.40.−z

I. INTRODUCTION

A granular material subjected to a slowly increasing external force often "fails" or "yields" [1,2]: after remaining nearly motionless, it suddenly starts to flow. This phenomenon is of both practical and fundamental interest. On the practical side, anyone who builds a house must be sure that the soil under the foundations will not yield. On the fundamental side, failure might be an example of a jamming transition and its characteristics may therefore be compared with those of the glass transition [3,4]. Yet failure poses several fundamental questions. First of all, what triggers failure? As the external load increases, small changes are always occurring inside the assembly, yet it does not yield. Finally, one change must trigger failure. Why does this particular change cause failure and not any of the preceding ones? Once the trigger is identified, the onset of failure is the problem of interest. How is the flowing motion initiated? What is its source of energy?

In this paper, we tackle these questions from a "structural mechanics perspective" [5]. One considers the granular assembly as a load-bearing structure and investigates its response to small changes in the load. Failure appears as an instability. Central to this approach is the stiffness matrix, which relates small displacements of the particles to changes in the force. This matrix can be analyzed to determine the stability of the assembly and thus to predict failure [5–9]. Furthermore, this matrix can be constructed for particles of arbitrary shape [5,6] and also for circular particles with both sliding and nonsliding contacts [9,10]. The stiffness matrix has been applied to failure in only a few limited cases: clusters of grains in a shear band [7] and a single particle stuck in a wedge-shaped channel [9]. The simplicity of this latter case permitted a detailed view of failure to be glimpsed. Failure is triggered by a change at a single contact that modifies how the packing responds to the external load. Using the stiffness matrix, one can explain how this change renders the assembly unstable.

Is this same process at work in larger, more complicated packings? To answer this question, we consider in this paper packings of 16 particles. This is an order of magnitude more than one particle, but still many orders of magnitude less than typical situations where we would like to understand failure. But these packings of 16 particles are a logical first step because they can be subjected to a detailed analysis. Specifically, the contact status changes can easily be separated in time enabling us to identify the ones that trigger failure. We hope that this knowledge can be exploited when treating larger assemblies, where, besides these phenomena, correlation effects might alter the behavior.

As described in Sec. II, we simulate assemblies of 16 particles contained in a biaxial box subjected to an increasing deviatoric stress. After a brief review of stiffness matrix theory in Sec. III, we study the effects of this increasing load in Sec. IV. In Sec. V, we identify the different events that trigger failure and analyze the onset of motion.

II. NUMERICAL PROCEDURE

A. Contact model

Grains are modeled as disks and their interactions are calculated using the common "soft-sphere molecular dynamics" method [11]. The force at the grain contact is generated by a linear dissipative spring whose length is given by the overlap distance D_n:

$$F_n = -k_n D_n - \gamma_n \dot{D}_n. \tag{1}$$

Here, k_n is the length-independent spring stiffness and the damping coefficient γ_n controls the damping. The overlap distance D_n is calculated from the radii r_i and r_j of the touching particles and their positions $\mathbf{x}_i$ and $\mathbf{x}_j$,

$$D_n = |\mathbf{x}_i - \mathbf{x}_j| - r_i - r_j. \tag{2}$$

When the surfaces of the two touching disks move relative to each other a second force F_t arises, directed tangent to the particle surfaces. In analogy with the normal force defined in Eq. (1) we have

$$F_t = -k_t D_t - \gamma_t \dot{D}_t. \tag{3}$$

In our case $k_t = k_n$ and $\gamma_t = \gamma_n$. Determining the change in the tangential spring length $\dot{D}_t$ involves both translational movement and rotation of the two touching particles i and j,

$$\dot{D}_t = -r_i \omega_i - r_j \omega_j + \frac{r_i + r_j}{r_i + r_j - D_n}(\mathbf{v}_i - \mathbf{v}_j) \cdot \mathbf{t}. \tag{4}$$

Here, ω_i and ω_j are the angular velocities of the touching particles and $\mathbf{t}$ is a vector tangent to the particle surfaces at the point of contact. The factor in front of the last term is needed to account for the overlap of the particles.

In our simulation we allow only for repulsive forces, $F_n > 0$. We also enforce the Coulomb condition at each contact,

$$\mu F_n \geq |F_t|. \tag{5}$$

At a given moment, contacts where the strict inequality holds are nonsliding contacts, whereas contacts with $\mu F_n = |F_t|$ are sliding.

B. Units and parameters

Three parameters are set to unity for all simulations: the particle density $\hat{\rho}$, the initial system length $\hat{L}$, and the pressure $\hat{p}$. This defines our system of units. In two dimensions, the unit of force is $\hat{f} = \hat{p}\hat{L}$ and the unit of energy is $\hat{E} = \hat{p}\hat{L}^2$. The unit of mass is $\hat{m} = \hat{\rho}\hat{L}^2$, whereas the time is measured in units of $\hat{t} = \hat{L}\sqrt{\hat{\rho}/\hat{p}}$. The spring stiffness, which is an important parameter in this paper, has a value of $k_{n,t} = 1600\hat{p}$. This leads to overlaps that are a small fraction of the radius: on average, we have $D_{n,t}/r \approx 0.3\%$. The damping is $\gamma_{n,t} = 6\hat{m}/\hat{t}$ and the Coulomb friction coefficient is $\mu = 0.25$. No gravity is applied to the particles.

C. Boundary conditions

We apply biaxial boundary conditions. These are easy to implement and simple to handle. In each direction, the granular packing is delimited by a lightweight (mass $0.01\hat{m}$) moveable wall parallel to one of the coordinate axes, as shown in Fig. 1. A force is applied to each boundary that can be constant or time dependent. In this way, one can fix the average stress inside the granular packing. The deformation of the packing can be determined by monitoring the movements of the boundaries. In our setup, the walls are perfectly slippery; i.e., they exert only normal forces. This has several advantages. First, the forces on opposite walls are guaranteed to be equal. Second, the number of degrees of freedom is reduced and last but not the least, larger systems are more homogeneous. The effect of boundary conditions will be assessed by comparing systems of different sizes in Sec. V F.
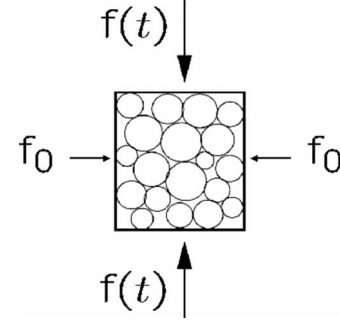

FIG. 1. Biaxial boundary conditions.

D. Preparation procedure

The two-dimensional granular medium is made up of disks with radii r uniformly distributed within the range [0.07, 0.1] and initial velocity in the range $v_x, v_y \in [-0.5, 0.5]$. The initial radii and velocities are chosen using a random number generator and a series of packings is generated by changing the "seed." The resulting assemblies obtained essentially differ in contact topology and the spatial distribution of the grain sizes. In this paper, we study a set of 26 different configurations of 16 disks.

The frictionless particles are initially separated, but a constant external force $f_0 = 0.8\hat{f}$ is applied to each of the walls, so that they move inward and compress the grains into a packing of approximate size $0.8\hat{L}$ capable of transmitting normal forces. During the compression process, kinetic energy is removed by the damping at particle contacts. Certain motions, however, require special care. For example, the velocity of the center of mass cannot be damped by contact forces, and thus a global viscous damping is applied for $10\hat{t}$. The kinetic energy decreases to $(6.9 \pm 0.1)10^{-8}\hat{E}$. The main reservoir of remaining kinetic energy is particles without contacts. To remove their energy, a viscous damping force opposing the individual grain movement is then applied for $40\hat{t}$ and the remaining kinetic energy is $(3.0 \pm 6.1)10^{-9}\hat{E}$. At the end of the preparation, friction is turned on.

E. Loading the sample

The configurations obtained are submitted to an increasing external force along the vertical axis, whereas the horizontally applied forces remain unchanged. The vertical force increase is linear,

$$f_{\text{ext},y}(t) = f_0 + \epsilon t. \tag{6}$$

To obtain a pressure $p = f_0/L$ that is approximately unity, we choose $f_0 = 0.8\hat{f}$. The prefactor ϵ determines the value of the very small force increment per time step. We wish to study failure in the quasistatic limit, meaning that the applied force at which the assembly fails is independent of ϵ. We checked that our simulations are quasistatic by performing runs with different load velocities (Fig. 2), and we choose $\epsilon = 1.28 \ 10^{-3}\hat{f}/\hat{t}$. At the beginning, a parabolic matching is applied to obtain a continuous differentiable force curve.
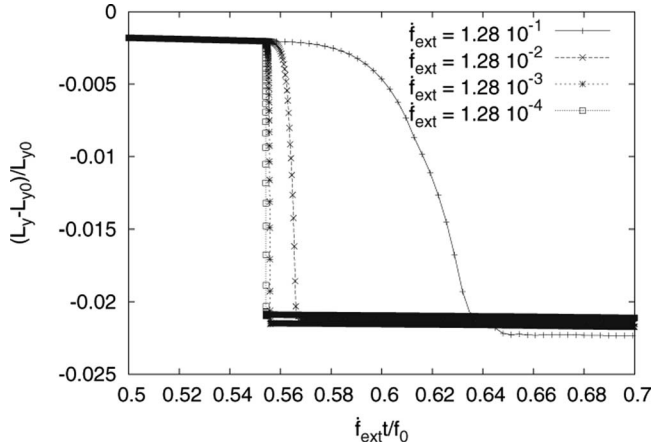
FIG. 2. Strain along the direction of the changing external force. Failure is characterized by a sudden change in strain. When the external force is changed slowly enough, (i.e., $df_{ext}/dt \leq 10^{-2}$) the time of failure depends solely on the critical value of the external force and not on its rate of change. During failure, the assemblies behavior is not quasistatic anymore, as can be seen from the different strain values attained thereafter.

III. THEORETICAL BACKGROUND

A. Rattlers

We begin our theoretical considerations by discussing a simple but frequent event that can complicate the analysis: it is possible for a grain to float inside a void, occasionally colliding with its neighbors. Such grains are called "rattlers." To some granular properties, rattlers contribute like other grains, e.g., the packing fraction of the granular assembly, where they contribute with a few percent. On the other hand, rattlers do not transmit forces and thus do not contribute to the load-bearing properties of the packing. Let us give an example: the stiffness of the granular assembly relates the change in external forces to the displacements of the walls. If rattlers are removed from the packing, then the stiffness will not change. Since rattlers do not contribute to the stiffness, we will remove them whenever we discuss the assembly's stability and refer in the following to the remaining number of grains as $\tilde{N}$.

B. Global hyperstatic number

Hyperstaticity is defined as the difference between the number of contact forces and the number of particle forces [12,13]. Here "contact forces" mean the normal and tangential forces at the contacts, and "particle forces" mean the total forces and torques exerted on the particles. In static equilibrium, the particle forces vanish, hence the contact forces must balance each other. When the number of contact forces is superior to the number of particle forces, the possible ways to choose the contact forces form a set whose dimension is called global hyperstatic number $\mathcal{H}$. Does $\mathcal{H}$ decrease with increasing deviatoric stress and vanish at the time when the packing collapses? We will discuss our simulation results in Sec. IV C.

To clarify the idea of hyperstaticity, we will first introduce a convenient representation of the forces. First, we group the forces in x and y directions, (f_x, f_y), and the torque τ, exerted on particle i, into a vector f_i. Then, we also group the normal and tangent contact forces at contact α, F_n, and F_t, into a vector F_α:

$$f_i = \begin{pmatrix} f_{i,x} \\ f_{i,y} \\ \tau_i/r_i \end{pmatrix}, \quad F_\alpha = \begin{pmatrix} F_{\alpha,n} \\ F_{\alpha,t} \end{pmatrix}. \tag{7}$$

Now we gather these quantities into a vector **f** for all $\tilde{N}$ particles and a vector **F** for all M contacts,

$$\mathbf{f} = \begin{pmatrix} f_1 \\ f_2 \\ \vdots \\ f_{\tilde{N}} \end{pmatrix} = \begin{pmatrix} f_{1,x} \\ f_{1,y} \\ \tau_1/r_1 \\ \vdots \\ f_{\tilde{N},x} \\ f_{\tilde{N},y} \\ \tau_{\tilde{N}}/r_{\tilde{N}} \end{pmatrix} \tag{8}$$

and

$$\mathbf{F} = \begin{pmatrix} F_1 \\ F_2 \\ \vdots \\ F_M \end{pmatrix} = \begin{pmatrix} F_{1,n} \\ F_{1,t} \\ \vdots \\ F_{M,n} \\ F_{M,t} \end{pmatrix}. \tag{9}$$

Note that the f_i are linearly related to the F_α, thus **f** is linearly related to **F**,

$$\mathbf{f} = \mathbf{cF}, \tag{10}$$

where **c** is a matrix that maps from the contact force space onto the particle force space [10].

In equilibrium, the particle forces **f** will balance the externally imposed forces $\mathbf{f}_{ext}$, $\mathbf{f} + \mathbf{f}_{ext} = 0$. In other words, the packing is stable when the equation

$$\mathbf{f}_{ext} = -\mathbf{cF} \tag{11}$$

has at least one solution. If the external forces are given, then Eq. (11) is simply a system of linear equations from which we can attempt to calculate the contact forces **F**. Let us investigate the possibility of solving this system. We begin by comparing the number of unknowns with the number of equations. On the left side of the equation we have three force components for each of the $\tilde{N}$ particles (rattlers are not considered), and also three components for the N_{walls} walls,

$$\mathcal{E}_p = 3(\tilde{N} + N_{walls}). \tag{12}$$

Now let us consider the number of contact forces. When all contacts are nonsliding, it is $\mathcal{E}_c = 2M$. But, when a contact becomes sliding, Eq. (5) tells us that $|F_t| = \mu F_n$, and the number of independent contact forces is reduced by one, because the tangential force can be derived from the normal one. Note that sliding contacts can slide only in one direction, whereas a motion in the other direction would cause the contact to become nonsliding. This might introduce a complica-

tion, which we do not take into account here. Thus the number of independent contact forces is reduced by the number of sliding contacts M_s,

$$\mathcal{E}_c = 2M - M_s. \qquad (13)$$

In our case, all contacts with the walls are always sliding because the walls are perfectly slippery. The dimension of the solution space of Eq. (11) is given by the *degree of hyperstaticity*,

$$\mathcal{H} = \mathcal{E}_c - \mathcal{E}_p + \mathcal{S}. \qquad (14)$$

$\mathcal{S}$ accounts for trivial free motions that appear due to the boundary conditions. First, the vector sum of the external forces on the walls is zero (no center of mass motion). This contributes two degrees of freedom to $\mathcal{S}$. Second, the tangential forces and the torques on the walls are zero (frictionless walls). This adds two trivial motions for each of the four walls to $\mathcal{S}$. Note that, on the contrary, a global rotation requires nonzero forces, as it implies that the walls are pushed outward while their orientations are fixed. Hence this is not a free motion and does not add to $\mathcal{S}$. We will see in Sec. V B that additional free motions can appear that add to $\mathcal{S}$. Sometimes, but not always, these motions trigger the collapse of the assembly.

When $\mathcal{H} > 0$, the granular assembly is hyperstatic, and the solution of Eq. (11) is not unique [12]. If $\mathcal{H} = 0$, the number of contact forces equals the particle forces, and the solution must be unique.

It has been shown by other authors [14,15] that assemblies of frictionless grains are isostatic in the limit of very low external forces or equivalently very high stiffnesses. The behavior of frictional assemblies, however, can be different [13,16,17]. We will discuss the degree of hyperstaticity observed in our simulations in Sec. IV C.

C. Quasistatic evolution

The degree of hyperstaticity characterizes static systems. In simulations one wishes to change external parameters and to study the system's response. In the quasistatic limit, a system's time-dependent properties (i.e., energy, forces, etc.) are independent of the rate at which any varying external parameter (e.g., stress) is changed. To be precise, one is interested to study a succession of static states $\mathcal{S}_1, \mathcal{S}_2, \ldots$ of the system that differ by small amounts in the external parameters $\mathcal{V}_1, \mathcal{V}_2, \ldots$. If the system is quasistatic, then each state $\mathcal{S}_i$ depends only on $\mathcal{V}_i$ (and possibly $\mathcal{V}_{i-1}, \mathcal{V}_{i-2}, \ldots$), but not on how fast the transitions between the preceding states are made.

In our case, the only varying external parameter is the magnitude of vertical external forces applied to the confining walls. It is slowly increased at a constant rate ϵ. In Fig. 2 we show the strain at failure for various ϵ. At $\epsilon = 1.28 \ 10^{-3} \hat{f}/\hat{t}$, the load at failure is very sharply defined and does not change when ϵ is reduced further. Thus we choose this value.

D. Stiffness matrix

1. Definition

Even in the quasistatic limit there will be small particle motions, because the slowly changing external force will be transmitted throughout the packing, introducing small displacements of all the grains toward a new equilibrium configuration. The equations that govern this motion can be written in matrix form [10]:

$$\mathbf{m}\ddot{\mathbf{v}} = \dot{\mathbf{f}}_{\text{ext}} - \mathbf{c}\mathbf{\Gamma}\mathbf{c}^T\dot{\mathbf{v}} - \dot{\mathbf{c}}\mathbf{F} - \mathbf{k}\mathbf{v}. \qquad (15)$$

Here, $\mathbf{m}$ is a diagonal matrix containing the masses and moments of inertia of all the particles. The vector $\mathbf{v}$ contains the velocities of the particles (both translational and angular) and is organized the same way as $\mathbf{f}$ in Eq. (8). The left-hand side is thus the accelerations of the particles differentiated once with respect to time.

On the right-hand side are the forces, again differentiated with respect to time. The first term is the change in the external forces and the second arises from the damping forces; the diagonal matrix $\mathbf{\Gamma}$ contains the damping coefficients and matrix $\mathbf{c}$ is the same as in Eq. (10). The last two terms express the change in the contact forces due to the change in position of the particles. A change in the geometry of the contact alters the direction of force transmission and this is described by the third term which constitutes the *geometric stiffness* of the assembly. This term is discussed in more detail in Appendix B. The last term is the change in contact forces due to the change in spring lengths and constitutes the *mechanical stiffness*. The matrix $\mathbf{k}$ is called the stiffness matrix and is determined by the geometry of the contact network and the contact statuses:

$$\mathbf{k} = \mathbf{c}\mathbf{K}\mathbf{S}\mathbf{c}^T. \qquad (16)$$

The geometry enters into matrix $\mathbf{c}$ [8–10] (see Appendix B), and the square matrix $\mathbf{S}$ contains all information about the contact statuses. Therefore matrix $\mathbf{S}$ is the only part that changes when contacts become sliding. If all contacts are nonsliding, matrix $\mathbf{S}$ is diagonal and of full dimension. But every sliding motion decreases this dimension, increasing the kernel by one dimension. Furthermore sliding contacts make matrix $\mathbf{S}$ become asymmetric. Matrix $\mathbf{K}$ is always diagonal and contains the contacts normal and tangential stiffnesses.

Equation (15) can be simplified under two assumptions. In the case of hard particles, the typical deformation D is much smaller than the particles radius r, $D \ll r$. This defines the so called *quasirigid limit*. The second assumption is that emerging vibrations are small enough so that their contribution to Eq. (15) can be neglected. This is the case if the lifetime of vibrations is significantly smaller than the frequency at which changes in the stiffness appear due to the change in external force, or alternatively when the vibrations can be separated from the slow deformation of the packing [10]. When this assumption, the so-called *quasistatic limit*, is also fulfilled, the last term on the right side is dominant:

$$\dot{\mathbf{f}}_{\text{ext}} = \mathbf{k}\mathbf{v}. \qquad (17)$$
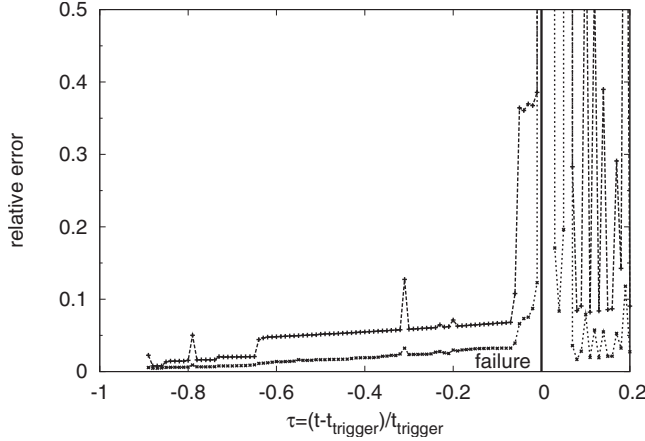
FIG. 3. Relative error of the stiffness matrix approach [Eq. (18)]. The figure shows the maximum error and the mean error of 26 assemblies from the beginning of the simulation at $\tau = -1$, through the failure at $\tau = 0$, and after failure. Note that failure lasts from $\tau = 0$ to about $\tau = 0.01$. One source of error are vibrations; they are especially important after failure has happened.

In this equation, the particle velocities only depend on $\dot{\mathbf{f}}_{ext}$ and $\mathbf{k}$ and they are completely independent of the grains' masses. Since $\dot{\mathbf{f}}_{ext}$ is constant and $\mathbf{k}$ only changes when a status change arises, the impact of such a contact status change can be noticed in a simultaneous sudden change in the velocity.

2. Accuracy of the stiffness matrix approach

We can check the validity of the assumptions leading to Eq. (17) by constructing the stiffness matrix $\mathbf{k}$, extracting $\mathbf{v}$ from the simulations, and calculating the relative error:

$$\Delta = \frac{|\dot{\mathbf{f}}_{ext} - \mathbf{k}\mathbf{v}|}{|\dot{\mathbf{f}}_{ext}|}. \tag{18}$$

Figure 3 shows the mean and maximum error for our granular assemblies. The values for $\tau < -0.9$ are not shown because they correspond to the beginning of the simulation where a parabolic force matching is applied (see Sec. II E). For $\tau < 0$ (before failure), the mean error is less than 5% and the maximum error is about 5% above this value. Close to $\tau = 0$, the maximum error rises sharply and attains 38.6%. During failure, which lasts until about $\tau = 0.01$, both the mean error and the maximum error are much higher. This is because some of the terms in the equations of motion that have been neglected in the derivation of Eq. (17) become important. After failure, vibrations lead to large errors, hence the average error remains large.

3. Particle velocities

If Eq. (17) could be solved for $\mathbf{v}$, the validity of the theory could be proven by comparing the result with the simulation velocities. However, $\mathbf{k}$ has no inverse, because certain motions, such as a translation of the system, lead to no change in the forces. Nevertheless, a pseudoinverse $\tilde{\mathbf{k}}$ of the stiffness

matrix can be defined that disregards these movements. We require that $\tilde{\mathbf{k}}\mathbf{k}\mathbf{v} = \mathbf{v}$ if $\mathbf{v}$ is orthogonal to the kernel of $\mathbf{k}$, and $\tilde{\mathbf{k}}\mathbf{k}\mathbf{v} = 0$ if $\mathbf{v}$ belongs to the kernel of $\mathbf{k}$. Then $\tilde{\mathbf{k}}$ can be used to predict the velocities $\mathbf{v}$:

$$\mathbf{v}_{th} := \tilde{\mathbf{k}}\dot{\mathbf{f}}_{ext}. \tag{19}$$

The index "th" indicates that the velocities are predicted theoretically. Our procedure for constructing $\tilde{\mathbf{k}}$ is described in Appendix A.

E. Stability

Now let us consider the stability of the packing. One criterion is [5–7,9]

$$\mathbf{v}\mathbf{k}\mathbf{v} > 0. \tag{20}$$

Note that whenever we write a matrix between two vectors, we mean that two scalar products are calculated, hence the result is a scalar. To be precise, we do not carry along the sign for the transposition of the left-hand side vectors.

Whenever the inequality in Eq. (20) is violated, instability will occur. When this happens, we have to re-evaluate the assumptions leading to Eq. (17). But let us first show which types of instability can occur. One possibility is

$$\mathbf{v}\mathbf{k}\mathbf{v} < 0. \tag{21}$$

When this equation is satisfied, a small displacement in the direction of $\mathbf{v}$ leads to a force that amplifies this displacement. A particular clear discussion of this is given in Ref. [5]. Another type of instability occurs when

$$\mathbf{v}\mathbf{k}\mathbf{v} = 0. \tag{22}$$

As discussed in Sec. III D 3, Eq. (22) always holds for some motions. It is therefore necessary to inspect the vectors $\mathbf{v}$: if they correspond to trivial motions, such as the uniform translation of all the particles, Eq. (22) does not signal failure, but simply expresses the translation invariance of space. On the other hand, if they correspond to nontrivial motions, then Eq. (22) indicates that the packing is unstable and fails.

The numerical results in the next few sections show that these statements must be nuanced. The reason for this is that the criteria in Eqs. (21) and (22) are based on Eq. (17), which in turn is based on the dominance of $\mathbf{k}\mathbf{v}$ over the other terms in Eq. (15). But as the load increases, $\mathbf{k}\mathbf{v}$ decreases, so that other terms may become important.

In the most common case the geometric stiffness becomes significant. In Eq. (15), it is written as $\dot{\mathbf{c}}\mathbf{F}$, but since $\dot{\mathbf{c}}$ is proportional to $\mathbf{v}$, it can be rewritten [5]:

$$\dot{\mathbf{c}}\mathbf{F} = \mathbf{k}_{geo}\mathbf{v}. \tag{23}$$

The stability of the packing depends on the total stiffness $\mathbf{k}_{tot} = \mathbf{k} + \mathbf{k}_{geo}$, and not just the mechanical stiffness $\mathbf{k}$. Thus, Eq. (21) should be modified to read

$$\mathbf{v}\mathbf{k}_{tot}\mathbf{v} = \mathbf{v}\mathbf{k}\mathbf{v} + \mathbf{v}\mathbf{k}_{geo}\mathbf{v} < 0. \tag{24}$$

The geometric stiffness is usually much smaller than the mechanical one for the reasons outlined in Appendix B. Hence

it represents a small correction to the total stiffness. But, it is always destabilizing in our simulations, so that it can cause a packing to fail even though it should be stable according to Eq. (20). The other term that can become important as **vkv** becomes small is the inertia term on the left-hand side of Eq. (15). At contact status changes, the velocities change and vibrations appear. The vibrations are a consequence of the inertia term. We will come back to this in Sec. IV E.

F. Kinetic energy during failure

Finally, we would like to understand what drives failure by analyzing the different sources of kinetic energy. When failure occurs, the grains begin to move and their kinetic energy increases. This kinetic energy must come from somewhere—it must either be injected into the system by the forcing or originate from the potential energy stored in the grains.

Let us begin by recalling the expression for the kinetic and potential energies:

$$E_{\text{kin}} = \frac{\mathbf{vmv}}{2}, \quad E_{\text{pot}} = \frac{\mathbf{DKD}}{2}. \quad (25)$$

Here, the diagonal matrix **K** contains the spring constants, and **D** is a vector containing the spring lengths, organized the same way as the contact forces in Eq. (9). We will consider the first and second derivatives of these quantities with respect to time. In addition, we will make use of Eq. (15), and Eq. (29) from [10],

$$\mathbf{m\dot{v}} = \mathbf{cF} + \mathbf{f}_{\text{ext}}. \quad (26)$$

To simplify the calculations, we will neglect the damping [**Γ** = 0 in Eq. (15)]. The first two derivatives of E_{kin} are

$$\dot{E}_{\text{kin}} = \mathbf{vm\dot{v}} = \mathbf{v}(\mathbf{f}_{\text{ext}} + \mathbf{cF}),$$

$$\ddot{E}_{\text{kin}} = \mathbf{\dot{v}m\dot{v}} + \mathbf{vm\ddot{v}}. \quad (27)$$

With Eqs. (15) and (26), the second derivative of the kinetic energy can be written as

$$\ddot{E}_{\text{kin}} = (\mathbf{f}_{\text{ext}} + \mathbf{cF})\mathbf{m}^{-1}(\mathbf{f}_{\text{ext}} + \mathbf{cF}) + \mathbf{v\dot{f}}_{\text{ext}} - \mathbf{vkv} + \mathbf{v\dot{c}F}. \quad (28)$$

The first term is the contribution from the force imbalance. As it is quadratic in $(\mathbf{f}_{\text{ext}} + \mathbf{cF})$, it is non-negative. The second term is the contribution from the increase in the external forces. The next two terms are related to the geometric and mechanical stiffnesses. This can be seen by comparing Eq. (28) with Eq. (15).

If one calculates the second derivative of the potential energy, and assumes all the contacts are nonsliding, one obtains

$$\ddot{E}_{\text{pot}} = -(\mathbf{cF})\mathbf{m}^{-1}(\mathbf{f}_{\text{ext}} + \mathbf{cF}) - \mathbf{v\dot{f}}_{\text{ext}} + \mathbf{vkv} - \mathbf{v\dot{c}F}. \quad (29)$$

We can combine Eqs. (28) and (29) to obtain

$$\ddot{E}_{\text{kin}} + \ddot{E}_{\text{pot}} = \mathbf{v\dot{f}}_{\text{ext}} + \mathbf{\dot{v}f}_{\text{ext}}. \quad (30)$$

This is simply a statement of the conservation of energy. During failure, the kinetic energy increases and the energy

TABLE I. Dependence of the energy contributions on **v** during failure. We used Eq. (26) to write **m$\dot{\mathbf{v}}$** for the forces appearing in the first line.

$|\mathbf{v}| \sim e^{\beta t/2}$	Contribution	Dependence	Key relation
Force imbalance	$\mathbf{\dot{v}m}^{-1}\mathbf{\dot{v}}$	$\sim vv$	$\mathbf{\dot{v}}/\mathbf{v} = \text{const}$
Change in load	$\mathbf{v\dot{f}}_{\text{ext}}$	$\sim v$	
Mech. stiffness	$-\mathbf{vkv}$	$\sim vv$	
Geometric stiffness	$\mathbf{v\dot{c}F}$	$\sim vv$	$\mathbf{\dot{c}} \sim v$

must come from the other terms. By calculating them, one can determine whether failure is driven by released potential energy or the external load.

We observe from the simulation results that E_{kin} always rises exponentially during failure: $E_{\text{kin}} \sim e^{\beta t}$. This means that the velocities must also increase exponentially. Failure is a collective rearrangement process, hence we can substitute the velocity vector by its length $|\mathbf{v}|$. Its time dependence is $|\mathbf{v}| \sim e^{\beta t/2}$.

If we consider the various terms in Eq. (28), we can determine which ones can drive failure. An exponential rise in E_{kin} is possible only if the dominate term on the right-hand side is also proportional to E_{kin}. Table I shows the dependence of all contributions on $|\mathbf{v}|$. Three of them are candidates for driving failure: the force imbalance, the mechanical stiffness, and the geometric stiffness. The last is proportional to E_{kin} because the change in contact geometry $\mathbf{\dot{c}}$ is proportional to the particle velocities, which is shown in Appendix B. The term $\mathbf{v\dot{f}}_{\text{ext}}$, arising from the change in the external load, is proportional only to $|\mathbf{v}|$, and thus is not capable of sustaining the exponential growth of the kinetic energy.

IV. LEADING UP TO FAILURE

In this section, we determine principal quantities of the granular packing describing its state on the way to failure. First of all, some contacts will become sliding when the external force is uniaxially increased. Their fraction increases on the way to failure. We also inspect the number of rattlers. It remains roughly constant. Then, we examine the degree of hyperstaticity. It decreases as the external load increases and becomes very small close to the failure. Finally, we discuss the stiffness of the packing that decreases as failure is approached.

The granular assemblies in this paper are small, therefore each of them will have its proper yield threshold. This threshold can be determined with precision because failure is always preceded by a contact status change that triggers failure. The time when this event occurs will be written as t_{trigger} and corresponds to a maximum dimensionless deviatoric stress $\mathcal{R}_{\text{trigger}} = [f(t_{\text{trigger}}) - f_0]/f_0$. To merge both the simulation beginning and the time of failure for the different assemblies, simulation results are plotted as a function of the rescaled time τ:

$$\tau = \frac{t - t_{\text{trigger}}}{t_{\text{trigger}}}. \quad (31)$$

When t approaches t_{trigger}, the time scale on which property changes occur will be much finer. Then we will use again the
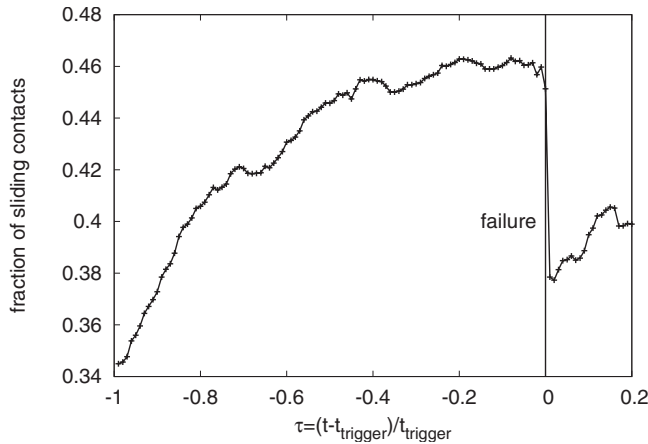
FIG. 4. Fraction of sliding contacts averaged over 26 different seeds. The fraction increases until the time when the assembly fails. During the deformation process, the fraction drops abruptly and the intergranular contacts stop sliding when the assembly attains a new stable state. The remaining fraction is the contacts with the smooth walls.
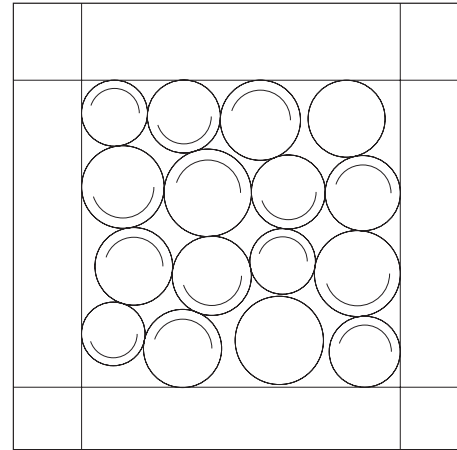

FIG. 5. Rotation mode with zero stiffness: whenever four grains form a square and touch each other, they rotate at the same speed but in opposite directions at their points of contact. (The rotations are indicated by the segment of a circle inside each grain; the segments start at the rightmost position and point in the direction of rotation. Their lengths indicate the speed.) Grains without indicated rotation are rattlers.

smaller simulation time units of $t - t_{\text{trigger}}$. Both time scales are centered around the time t_{trigger} where the trigger mechanism occurs. Its average is $t_{\text{trigger}} = 734 \pm 436 \hat{t}$ and the maximum dimensionless deviatoric stress is $\mathcal{R}_{\text{trigger}} = 1.08 \pm 0.70$.

A. Sliding contacts

When we increase the deviatoric part of the external stress on the packing, the number of sliding contacts rises [18,19], as shown in Fig. 4. The number of sliding contacts increases linearly for $\tau < -0.8$, but then this increase slows. From $\tau > -0.1$ until the time of failure, the number of sliding contacts is approximately constant.

When the granular assembly fails, many contact rearrangements occur leading to fluctuations in the number of sliding contacts that are not resolved in the above figure. After failure, all grain-grain contacts will become nonsliding again and only the contacts with the smooth walls contribute to the value in Fig. 4. When the external force is increased further, the number of sliding contacts rises again.

B. Fraction of rattlers

The principal question is whether or not the occurrence of rattlers is related to the failure of granular material. One can imagine that rearrangement processes will occasionally force grains to stay without any contact to their surrounding neighbors. But our results tell us that on average already one rattler exists at the beginning of the simulation. One origin could be the rigid boundary conditions that we apply. Imagine a system of 16 equally sized particles on a square lattice confined by four walls, then 12 of the 16 particles will touch the walls. Now let some of the particles shrink whereas other are allowed to grow in radius. In this system it happens that one of the grains is "trapped" in a region enclosed by other particles and the walls, but stays without contacts. Two of such rattlers are shown in Fig. 5. The number of rattlers stays

constant during the simulation and increases only slightly through the rearrangement process. Hence, rattlers are not important for failure.

C. Global hyperstatic number

The graph of the number $\mathcal{H} = \mathcal{E}_c - \mathcal{E}_p + \mathcal{S}$ of the degree of hyperstaticity, averaged over the granular assemblies investigated, is shown in Fig. 6. At the beginning of the simulation, the granular assemblies are hyperstatic with $\mathcal{H} = 6.3$ on average. When the deviatoric strain is increased as indicated in Fig. 1, the value decreases rather quickly in the beginning, but this change slows significantly when approaching the time when failure occurs. The data plotted in the graph are too coarse to show what happens at the time of failure.

The lower graph in Fig. 6 shows the degree of hyperstaticity close to the trigger mechanism. Before the trigger occurs, the granular assemblies are on average hyperstatic. Through the trigger at $t = t_{\text{trigger}}$, the average $\overline{\mathcal{H}}$ falls by 0.3 units and immediately attains its minimum value. This indicates that the trigger event is the essential mechanism that renders the granular assembly unstable. Shortly thereafter $\mathcal{H}$ increases slightly. In the interval after t_{trigger}, which constitutes the region when the granular assembly starts to fail, the average of $\mathcal{H}$ does not change significantly.

In all of the assemblies investigated we find values of $\mathcal{H}$ close to zero, showing that the number of "excess" contact forces is very small. We imagine two effects that make the value of $\overline{\mathcal{H}}$ somewhat noisy. First, there are, in certain cases, movements not leading to failure but involving all the grains, as discussed in Sec. III D 3 and shown in Fig. 5. Second, not all of the grains must necessarily move relative to each other when the assemblies fail. There might be just a few grains that displace at one common velocity but relative to the other grains in the assembly. Indeed, we observed that in larger
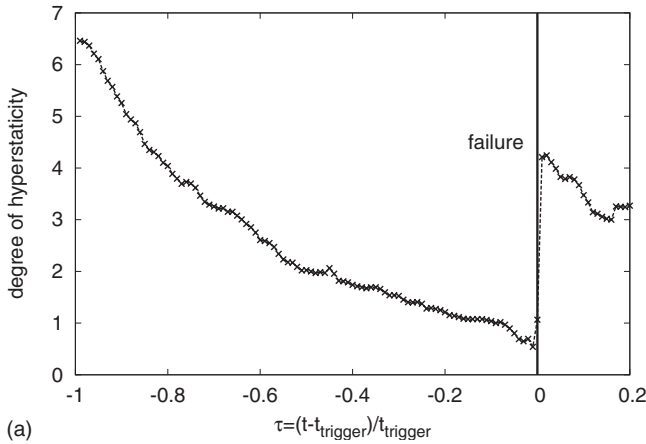
(a)
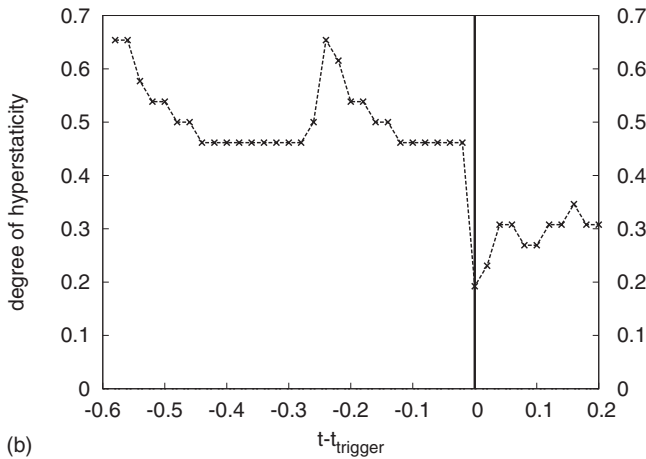
(b)

FIG. 6. Degree of hyperstaticity averaged over 26 different seeds. (a) Values from the beginning of the simulation until after failure. (b) Values for a small time interval around the trigger event. When a contact status change triggers the collapse, this leads on average to a decrease in the degree of hyperstaticity. Note that one time unit in the second figure is on average 1/500 of a unit in the first figure, hence the period covered by the entire second figure corresponds to less than the thickness of the vertical line in the first figure.

systems rearrangements mainly organize in shear bands, and $\mathcal{H}$ is significantly above zero at all times.

We did not pursue the evaluation of $\mathcal{H}$ at the granular scale, but leave this point for future investigations. Based on the diversity of individual behavior, we conclude that the absence of hyperstaticity $\mathcal{H}=0$ is not a global property of granular assemblies at failure. Rather, it is necessary to identify special regions where failure is initiated (such as in the shear band).

D. Softening of the granular assembly

On the macroscopic scale the stiffness can be measured from the response of the walls to the force increment. When we increase the forces, the deviatoric stress also increases at the rate

$$\dot{\sigma}_D = \frac{\dot{f}_{\text{ext},y}}{L_x}. \tag{32}$$
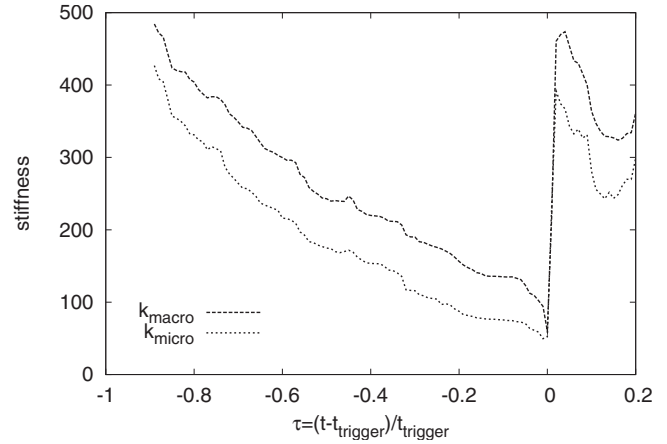
The deviatoric strain is

FIG. 7. Comparison of the macroscopic and microscopic stiffnesses. The macroscopic stiffness is calculated from the response of the confining walls according to Eq. (34). The microscopic stiffness is calculated using $\dot{\mathbf{f}}_{\text{ext}}$ and $\mathbf{v}$ according to Eq. (35).

$$\epsilon_D = \frac{\Delta L_y}{L_y} - \frac{\Delta L_x}{L_x}. \tag{33}$$

One measure of the stiffness is thus

$$k_{\text{macro}} = \frac{\dot{\sigma}_D}{\dot{\epsilon}_D}. \tag{34}$$

On the other hand, we can estimate the stiffness on the microscopic scale:

$$k_{\text{micro}} = \frac{|\dot{\mathbf{f}}_{\text{ext}}|}{|\mathbf{v}|}. \tag{35}$$

An expression for k_{micro}, based on the stiffness matrix, can be established by first defining the normalized vectors $\mathbf{n}_{\dot{f}_{\text{ext}}} = \dot{\mathbf{f}}_{\text{ext}}/|\dot{\mathbf{f}}_{\text{ext}}|$, and $\mathbf{n}_v = \mathbf{v}/|\mathbf{v}|$, and then multiplying Eq. (17) from the left by $\mathbf{v}/\mathbf{vv}$. Note that $\mathbf{vv}$ is scalar. One thus obtains

$$k_{\text{micro}} = \mathbf{n}_{\dot{f}_{\text{ext}}} \mathbf{k} \mathbf{n}_v \approx \left(\frac{\mathbf{vkv}}{\mathbf{vv}} \right) \frac{1}{\mathbf{n}_{\dot{f}_{\text{ext}}} \mathbf{n}_v}. \tag{36}$$

The quadratic form $\mathbf{vkv}$ that appears in the microscopic stiffness is the essential term in the stability criteria presented in Sec. III E, and a negative or vanishing stiffness leads to failure. The mean value of $\mathbf{n}_{\dot{f}_{\text{ext}}} \mathbf{n}_v$ is 0.09 showing that the part of $\mathbf{v}$ parallel to $\dot{\mathbf{f}}_{\text{ext}}$ is small. Note that Eqs. (35) and (36) are furthermore not identical because Eq. (36) assumes Eq. (17), whereas Eq. (35) does not.

Figure 7 shows stiffness values calculated from different definitions. They exhibit the same qualitative time dependence: when we approach the onset of failure, the granular assembly will get much softer and attain its minimum value around $\tau=0$. As we will see in the next section, the stiffness drops sharply at the time of failure, but the time scale in Fig. 7 is too coarse to reveal this. After the failure, stability is soon fully recovered.
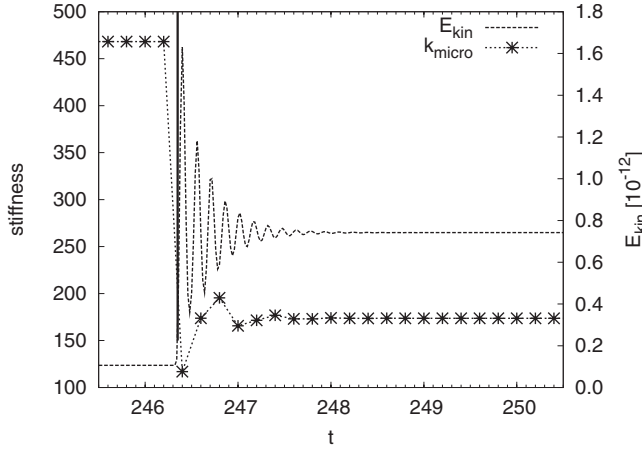
FIG. 8. A close view of a status change. At $t \approx 246.35$, a contact becomes sliding. Both the stiffness and the kinetic energy make a steplike change accompanied by damped oscillations.

E. Stiffness transitions

Figure 7 is an average over 26 simulations and should not lull one into thinking that the stiffness decreases smoothly and continuously in the simulations. In fact, the stiffness increases and decreases stepwise and the steps correspond to contact status changes. Whereas for the frictionless grains contacts can only open or close, friction makes possible four additional transitions, two from sliding to the other states and two vice versa. For both, frictional or frictionless particles, the steps correspond to contact status changes. In Fig. 8, we show one such event, where a contact becomes sliding at $t \approx 246.35\hat{t}$. Both before and after this event, the stiffness and the kinetic energy are constant, and the status change causes the stiffness to drop to a new level, while the kinetic energy rises. If the system was perfectly quasistatic, the transition would be instantaneous and without oscillation. To understand these oscillations in detail, let us use stiffness matrix theory. When the contact becomes sliding, there is an abrupt change in certain elements of the stiffness matrix, i.e., one has $\mathbf{k}=\mathbf{k}_1$ for $t<246.35\hat{t}$, and $\mathbf{k}=\mathbf{k}_2$ for $t>246.35\hat{t}$. Applying Eq. (17) gives $\dot{\mathbf{f}}_{\text{ext}}=\mathbf{k}_1\mathbf{v}_1=\mathbf{k}_2\mathbf{v}_2$, for $\dot{\mathbf{f}}_{\text{ext}}$ is constant. At $t=246.35\hat{t}$, therefore, Eq. (17) predicts an instantaneous change in the velocities. But the particles have a finite inertia and cannot change their velocities instantaneously. The status change in Fig. 8 is thus accompanied by a disturbance that is damped out after roughly ten oscillations or $1.5\hat{t}$. The disturbance is accounted for by the inertia term $\mathbf{m}\ddot{\mathbf{v}}$ and the damping term $\mathbf{c}\mathbf{\Gamma}\mathbf{c}^T\dot{\mathbf{v}}$ in Eq. (15). If these terms are included, the equation of motion thus becomes

$$\mathbf{m}\ddot{\mathbf{v}} = \dot{\mathbf{f}}_{\text{ext}} - \mathbf{c}\mathbf{\Gamma}\mathbf{c}^T\dot{\mathbf{v}} - \mathbf{k}\mathbf{v}, \tag{37}$$

which is a vectorized version of a damped harmonic oscillator. This explains the damped oscillations present in Fig. 8.

We include this detailed discussion of an example of a stiffness transition, because the vibrations involved therein will become important again in Sec. V C. We will now turn our attention to failure itself.
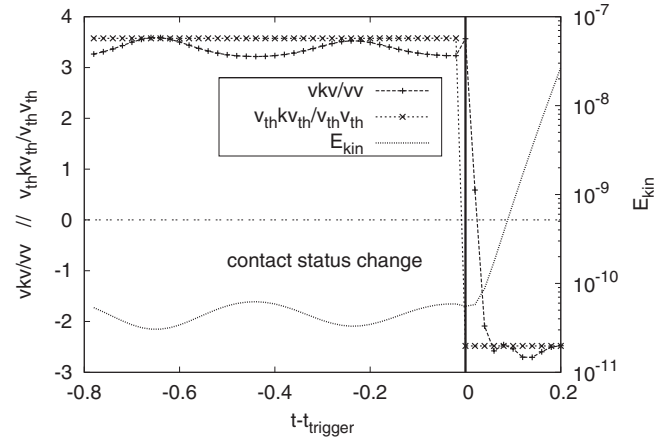

FIG. 9. Mechanical instability at the origin of failure: when the contact status change occurs, the stiffness, represented by $\mathbf{vkv}/\mathbf{vv}$, decreases rapidly and finally attains negative values. The purely structure-dependent quantity $\mathbf{v_{th}kv_{th}}$ changes instantaneously and hence shows the effect of the contact status change at the vertical line, whereas the simulation velocities $\mathbf{v}$ change on a time scale related to the particle inertia.

V. TRIGGERING FAILURE

Before the grains velocities start to rise, there is always a contact status change that leads to a change of the stiffness matrix $\mathbf{k}$. This change provokes the collapse of the assembly. Three different trigger mechanisms can occur: first, a contact status change can lead to a "negative stiffness" of the contact network, i.e., $\mathbf{vkv}<0$. Second, a null mode can cause the violation of Eq. (17) due to the loss of mechanical stability. Finally, there is a third possibility not foreseen in Ref. [9]: the packing can become unstable as it makes a transition between two different stable states.

A. Mechanical instability ($\mathbf{vkv}<0$)

When the quadratic form $\mathbf{vkv}$ becomes negative, the assembly becomes unstable for the reasons discussed in Sec. III E. In Fig. 9, we show data from one simulation where this happens. There is a contact status change at $t=t_{\text{trigger}}$, which provokes a drop in $\mathbf{vkv}$. But, as can be seen in the figure, it takes a finite time for $\mathbf{vkv}$ to become negative and for the kinetic energy to start to rise exponentially.

We can show the drop in $\mathbf{vkv}$ is caused by the contact status change by calculating $\mathbf{v_{th}kv_{th}}$, where $\mathbf{v_{th}}$ is given in Eq. (19). This quantity reveals the correspondence of contact status change and velocity adjustment because it instantaneously changes (see Sec. III D 3). On the other hand $\mathbf{vkv}$ is calculated using the velocities $\mathbf{v}$ from the simulation. The particle masses $\mathbf{m}$ in Eq. (15) define the time scale needed for $\mathbf{v}$ to change. Also, $\mathbf{v}$ oscillates before failure indicating the presence of vibrations. In any case, however, it is clear that the contact status change provokes an instability in the packing causing it to fail.

To understand more fully the mechanism of failure, let us examine the various contributions to the second derivative of the kinetic energy shown in Fig. 10. Before failure occurs, there is an equilibrium between three terms. The energy in-
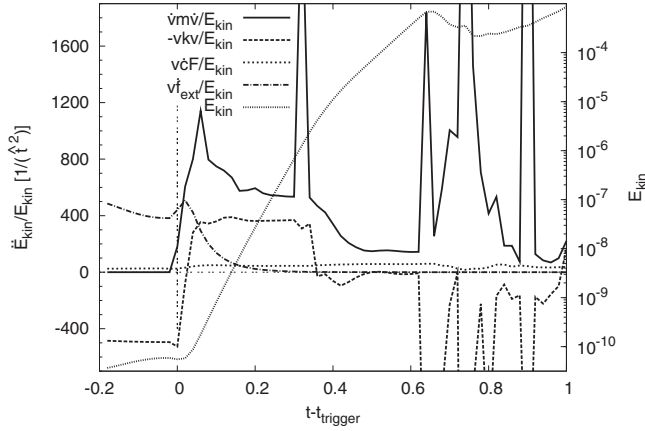
FIG. 10. Contributions to $\ddot{E}_{kin}$, and E_{kin}, for the simulation shown in Fig. 9, where an instability triggers failure. The contributions to $\ddot{E}_{kin}$ are plotted on a linear scale, indicated on the left, while E_{kin} is plotted on a logarithmic scale shown on the right. $\dot{\mathbf{v}}\mathbf{m}\dot{\mathbf{v}}$ is the contribution from the force imbalance.

jected by the external forcing ($\mathbf{v}\dot{\mathbf{f}}_{ext}$) and the geometric stiffness ($\mathbf{v}\dot{\mathbf{c}}\mathbf{F}$) contribute to the kinetic energy. This energy is removed by the mechanical stiffness ($\mathbf{v}\mathbf{k}\mathbf{v}$).

At $t=t_{trigger}$, a contact status change occurs and $\mathbf{v}\mathbf{k}\mathbf{v}$ begins to decrease toward 0. It can no longer absorb the energy injected by the other two terms and the kinetic energy starts to rise. A short time later, the force imbalance ($\dot{\mathbf{v}}\mathbf{m}\dot{\mathbf{v}}$) rises and becomes the dominant source of kinetic energy throughout the rest of the failure. At $t=t_{trigger}+0.7$, the kinetic energy reaches a maximum, more than 4 orders of magnitude above its initial value. The system then starts to search for a new equilibrium configuration.

B. Null-mode trigger

The second failure mechanism that can occur is the disappearance of mechanical rigidity. This means that there is some motion $\mathbf{v}_0$ to which the packing opposes no resistance. This occurs when the dimension of the kernel of $\mathbf{k}$ increases due to a contact status change and $\mathbf{v}_0$ is the dimension that has been added to the kernel. If $\mathbf{v}_0$ is compatible with the boundary conditions, then its amplitude will grow rapidly.

In Fig. 11, we show the data from a simulation where failure is triggered by the appearance of a null mode. At $t=t_{trigger}$, there is a contact status change that causes the kernel of $\mathbf{k}$ to increase by one dimension. This was determined by constructing $\mathbf{k}$ both for and after the contact status change and then carrying out a singular value decomposition. Note that the behavior of $\mathbf{v}\mathbf{k}\mathbf{v}$ is similar to Fig. 9: it drops sharply at $t=t_{trigger}$. On the other hand, $\mathbf{v}_{th}\mathbf{k}\mathbf{v}_{th}$ behaves quite differently because these two quantities diverge at $t=t_{trigger}$. The reason for this will be discussed below.

In Fig. 12, we show the new null mode that appears at the contact status change. As one can see, it corresponds to a crushing of the granular assembly between the upper and lower walls, which is exactly the kind of motion expected at failure. In the figure, the top row is moving to the right, and the second row to the left, meaning that the top row will slip
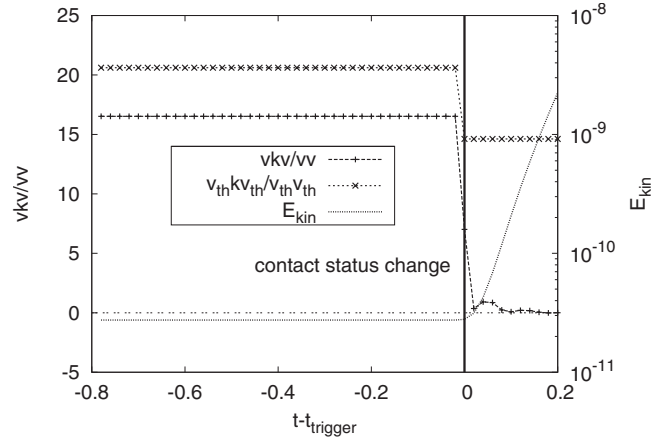

FIG. 11. Stiffness of the granular assembly ($\mathbf{v}\mathbf{k}\mathbf{v}/\mathbf{v}\mathbf{v}$) at failure caused by the appearance of a null mode. The thick vertical line at $t=t_{trigger}$ shows the time when the null mode appears due to a contact status change.

down into valleys formed by the second row, so that the packing will go roughly from square to triangular. The sliding contacts are marked by gray or black circles, with the black circle indicating the contact that becomes sliding when the null mode appears.

Further evidence of the null-mode failure is shown in Fig. 13, where the fraction of the velocity attributed to the null mode is plotted. It rises rapidly at the contact status change and quickly dominates the motion. This figure also explains the divergence of $\mathbf{v}\mathbf{k}\mathbf{v}$ and $\mathbf{v}_{th}\mathbf{k}\mathbf{v}_{th}$ in Fig. 12. After failure, we have $\mathbf{v}\approx\mathbf{v}_0$, so that $\mathbf{k}\mathbf{v}\approx\mathbf{0}$. On the other hand, $\mathbf{v}_{th}$ is orthogonal to $\mathbf{v}_0$ by construction. Thus calculating $\mathbf{v}_{th}$ misses failure completely. This should be kept in mind whenever the stiffness matrix is used to calculate the motion of the packing.

Another subtlety is that the presence of a null mode is not sufficient to cause failure. Figure 5 shows an example of a
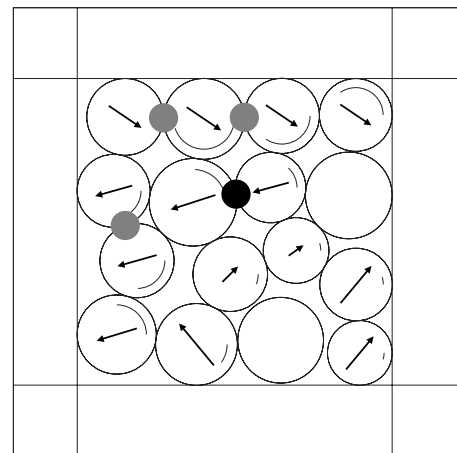

FIG. 12. The null mode that triggers failure in Fig. 11. Velocities are indicated by arrows and angular velocities are represented by a circle segment inside the corresponding grain. Grains for which no velocity is shown are rattlers. When the null mode occurs, the contact marked by the black circle starts to slide. The other sliding contacts are indicated by gray circles.
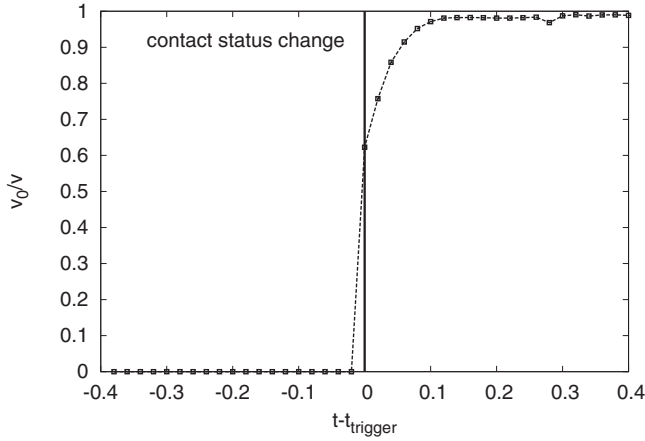
FIG. 13. Fraction of the particle velocity **v** associated with the null mode $\mathbf{v}_0$ at failure for the simulation shown in Fig. 11. Shortly after the contact status changes, the velocity vector points in the direction of the null-mode movement, i.e., $\mathbf{v}\mathbf{v}_0/|\mathbf{v}||\mathbf{v}_0| \approx 1$.

null mode that does not cause failure. It is a global rotation mechanism, in which the assembly consists of loops comprising four grains. In these loops, the grains in contact rotate opposite to each other and the absolute value of angular rotation times the grains radius is a constant for all the grains. No friction opposes this movement, and hence the energy stored in the rotation remains unchanged until it will be converted back to potential energy at the time when this null mode disappears due to an opening or closing contact.

Another issue is the increase in kinetic energy after failure. As shown in Fig. 14, the kinetic energy rises exponentially but it is not clear why this should happen. If one assumes that the null mode is independent of the other motions, the kinetic energy should rise with the fourth power of time (see Appendix D) [9]. For certain examples of null mode failure, it is possible to fit the beginning of the curves of kinetic energy to polynomials of the form At^4+Bt^2+C, where the coefficients obey the scalings predicted in Appen-
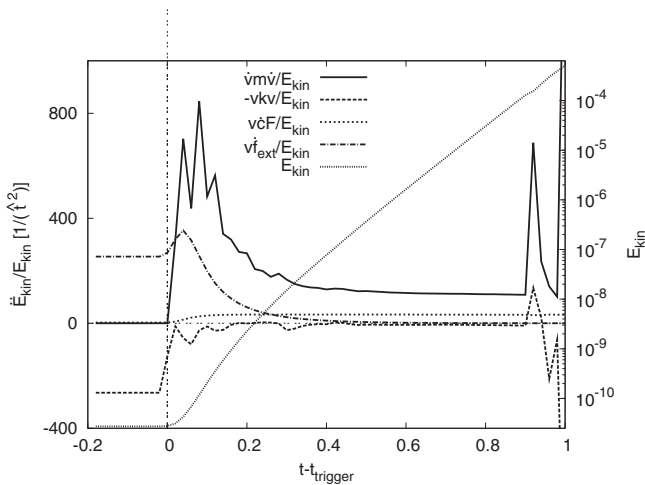

FIG. 14. Contributions to $\ddot{E}_{\text{kin}}$ and E_{kin}, for the simulation shown in Fig. 11, where a null mode triggers failure. The contributions to $\ddot{E}_{\text{kin}}$ are plotted on a linear scale, indicated on the left, while E_{kin} is plotted on a logarithmic scale shown on the right.
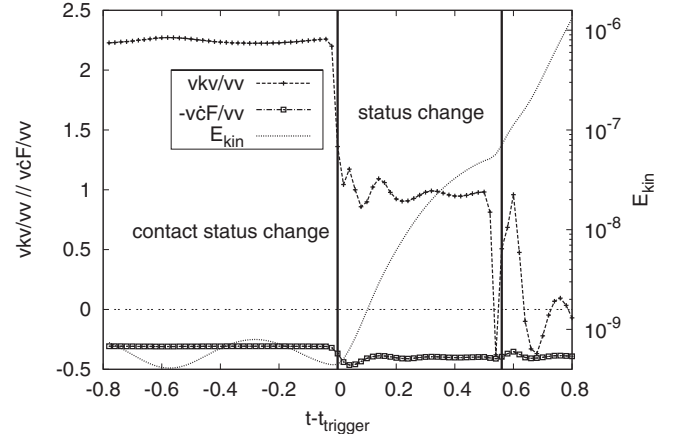

FIG. 15. An example of an ambushed transition: the kinetic energy starts to rise at $t=t_{\text{trigger}}$, even though the packing is stable.

dix D. However, the kinetic energy then soon rises exponentially. The reason for this can be seen in Fig. 14: the force imbalance becomes large. Why this would happen is puzzling at first sight because the null mode should not change the forces by definition. However, all these considerations neglect the geometric stiffness, which is always destabilizing. Hence, $\ddot{E}_{\text{kin}}$ contains only positive contributions. Therefore, the kinetic energy injected by geometric stiffness ($\mathbf{v}\dot{c}\mathbf{F}$) and external forcing ($\mathbf{v}\dot{f}_{\text{ext}}$) generates the force disequilibrium, which in turn generates the exponential growth of kinetic energy.

C. Ambushed transitions

In four out of the 26 simulations, failure seems to begin before an instability has appeared. One example is shown in Fig. 15. There is a contact status change at $t=t_{\text{trigger}}$ and the energy begins to rise. The packing, however, is stable. As one can see, $\mathbf{v}\mathbf{k}\mathbf{v}>0$, and it is large enough to dominate the geometric stiffness. Furthermore, no null modes are present. Note, however, that the increase in kinetic energy is slower than exponential for $t-t_{\text{trigger}}<0.5$. At around $t-t_{\text{trigger}}=0.5$, a second status change occurs and the energy then rises exponentially.

We believe that the initial increase in the kinetic energy is due to an oscillation associated with a stiffness transition very similar to the one shown in Fig. 8. At $t-t_{\text{trigger}}=0.5$, an instability appears and it is this instability that causes failure. We call this phenomenon an "ambushed transition," because there is first a transition from one stable state to another one. But during the very short transition period, an instability occurs. Thus, the initial rise in kinetic energy is due to a transition, but it is the instability that finally causes it to become very large.

When the stiffness is very low, vibrations of very low frequency often occur. These are damped insufficiently and are therefore long lasting. Note that the stiffness for $0<t-t_{\text{trigger}}<0.5$ is extremely low: $\mathbf{v}\mathbf{k}_{\text{tot}}\mathbf{v}\approx 0.5$. Two of the other three simulations displaying ambushed transitions also exhibit a very low stiffness, with $(\mathbf{v}_{\text{th}}\mathbf{k}\mathbf{v}_{\text{th}})/(\mathbf{v}_{\text{th}}\mathbf{v}_{\text{th}})<1$. This is
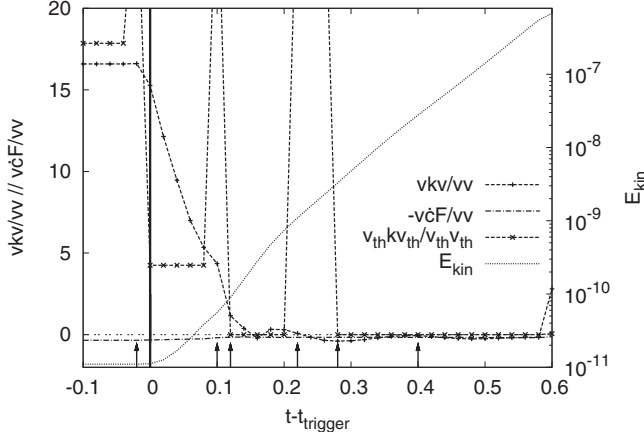
FIG. 16. The most difficult example of failure to classify. The triggering event is shown by a heavy vertical line. Other contact status changes are shown by the short vertical arrows at the bottom of the graph. At certain short periods of time, a null mode exists. When this occurs, $(\mathbf{v}_{th}\mathbf{k}\mathbf{v}_{th})/(\mathbf{v}_{th}\mathbf{v}_{th})$ jumps to a value near 30.

smaller than the stiffness observed in all the other stable configurations.

However, one case did not fit this pattern. It is shown in Fig. 16. The kinetic energy begins to grow rapidly, even though the packing is still stable. Note that $(\mathbf{v}_{th}\mathbf{k}\mathbf{v}_{th})/(\mathbf{v}_{th}\mathbf{v}_{th}) \approx 4$ just after $t_{trigger}$, a value we could observe in other stable packings as well. One example can be seen in Fig. 9, where $(\mathbf{v}_{th}\mathbf{k}\mathbf{v}_{th})/(\mathbf{v}_{th}\mathbf{v}_{th}) \approx 4$ *before* failure. We therefore checked if the initial energy rise was part of an oscillation by running the same simulation with $\dot{\mathbf{f}}_{ext}$ reduced by a factor of 10. When this is done, the status change at $t - t_{trigger} \approx 0.1$ is postponed until $t - t_{trigger} \approx 0.5$. Shortly before the second status change, the kinetic energy starts to decrease showing that the first rise in energy is part of an interrupted oscillation.

Changing $\dot{f}_{ext}$ also allows us to see that this failure mechanism is not purely quasistatic, for if it were, the instability would arise always at the same value of f_{ext}. But when $\dot{f}_{ext}$ is reduced, failure occurs at a smaller value of f_{ext}. Thus the oscillation plays an essential role in failure. On the other hand, if the appearance of the instability depended only on the oscillation, the separation in time between the two status changes would not change. But we observe that this time does indeed change. Thus both the oscillation and the value of f_{ext} have a role.

Another question is the curious nature of some of the transitions in Fig. 16. For example, just before failure, the curve $(\mathbf{v}_{th}\mathbf{k}\mathbf{v}_{th})/(\mathbf{v}_{th}\mathbf{v}_{th})$ shoots up to about 30, off the scale of the graph, and then suddenly drops down to about 5. This is not an error but a sign of a null mode that appears rapidly and then disappears. Such compound transitions are discussed in the next section.

D. Compound status changes

Figure 16 illustrates another phenomenon that is sometimes observed: a sequence of status changes. Apart from the contact status change at $t = t_{trigger}$, several other events are
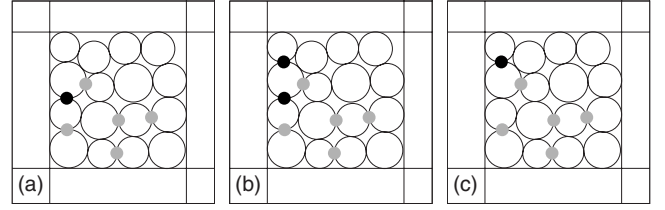

FIG. 17. Compound status change. The compound status change involves the two contacts in the upper left corner marked with the black circles when they are sliding. The other sliding contacts are marked with gray circles. The pictures are taken at $t - t_{trigger} = -0.04, -0.02, 0$ (from left to right).

indicated by short vertical arrows at the bottom of the figure. These events can also be seen from $(\mathbf{v}_{th}\mathbf{k}\mathbf{v}_{th})/(\mathbf{v}_{th}\mathbf{v}_{th})$: when this quantity jumps upward to a value above the top of the graph, a null mode has appeared and when it returns to a lower value, that null mode disappears. Each appearance and disappearance is associated with a contact status change.

To understand what is happening, Fig. 17 shows the sequence of contact status changes until $t = t_{trigger}$ in Fig. 16. The transition as a whole involves a shift in the location of a single sliding contact. The system passes between these two states via a third state in the middle panel, where both contacts are sliding. Each of the three states corresponds to a different stiffness: the left-hand state is relatively stiff and corresponds to $(\mathbf{v}\mathbf{k}\mathbf{v})/(\mathbf{v}\mathbf{v}) \approx 17$ ($t - t_{trigger} < -0.02$ in Fig. 16), the middle to the existence of a null mode ($t - t_{trigger} = -0.02$), and the last state to a reduced stiffness of $(\mathbf{v}\mathbf{k}\mathbf{v})/(\mathbf{v}\mathbf{v}) \approx 4$ ($t = t_{trigger}$).

Such "compound contact status changes" are observed several other times in Fig. 16 and occasionally in other systems. In Fig. 16, a compound contact status change is involved in an ambushed transition, but no such general relation exists: ambushed transitions and compound status changes occur independently of each other.

E. Statistical evaluation

We examined each of the 26 assemblies to determine the trigger type. First, we identify the contact status change that triggers failure by examining the simulation data at the point where the energy starts to grow. Then we inspected the change in $\mathbf{v}\mathbf{k}\mathbf{v}$ and $\mathbf{v}_{th}\mathbf{k}\mathbf{v}_{th}$ at the trigger event. If $\mathbf{v}_{th}\mathbf{k}\mathbf{v}_{th}$ becomes negative at the trigger event, and $\mathbf{v}\mathbf{k}\mathbf{v}$ converges to $\mathbf{v}_{th}\mathbf{k}\mathbf{v}_{th}$ after a short time, then the trigger is classified as an instability. An example is shown in Fig. 9. Simulations where $\mathbf{v}\dot{\mathbf{c}}\mathbf{F} > \mathbf{v}\mathbf{k}\mathbf{v} > 0$ are also classified as an instability, because the total stiffness is negative.

Next the possibility of null-mode failure must be considered. This is done by performing a singular value decomposition on $\mathbf{k}$ and checking if the number of null modes increases at $t_{trigger}$. Then the null mode must be consistent with boundary and load conditions. If $(\mathbf{v}\mathbf{k}\mathbf{v})/(\mathbf{v}\mathbf{v})$ and $(\mathbf{v}_{th}\mathbf{k}\mathbf{v}_{th})/(\mathbf{v}_{th}\mathbf{v}_{th})$ diverge from one another, the null mode will trigger failure. Alternatively, one can check if $\mathbf{v}_0\mathbf{v}/(|\mathbf{v}_0\|\mathbf{v}|) = 1$.

There are four simulations that could not be classified in this way. These systems display "ambushed transitions" and were discussed in Sec. V C.
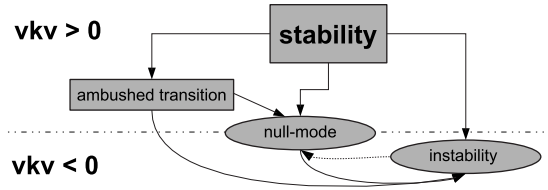
FIG. 18. Relation of trigger mechanisms. All systems begin in the box marked "stability." Then they can fail through three different ways indicated by the three arrows emerging from this box. The remaining arrows indicate that transitions are sometimes possible between different mechanisms. Though we did not observe the transition from the box "instability" to the "null-mode" oval, we do not want to claim it is not possible. The dotted horizontal line indicates $\mathbf{vkv}=0$.

It should be remarked that it was not clear how to classify some of the simulations. In three of them, first a null mode is present then a weak instability appears. These three simulations were all classified as null mode, because the kinetic energy increases significantly before the instability appears.

In our 26 assemblies, an ambushed transition occurs four times, whereas the null-mode trigger was observed 14 times. Instability is at the origin of failure in eight assemblies. These results suggest that ambushed transitions are rather rare, whereas the null-mode trigger frequently occurs in the small systems.

One can also ask what kind of contact status changes causes failure. In 13 of 26 assemblies, a contact begins to slide (in one case two contacts become sliding). In eight other assemblies one or more contacts open when the trigger occurs, and in another three assemblies one contact closes at that time. In the two remaining assemblies two different contact status changes happen at the same time: in one assembly a sliding contact became nonsliding and another sliding contact opened, and in the other assembly one open contact became sliding while a different sliding contact opened. The statistics suggest that at the origin of the trigger usually at least one contact opens or starts to slide.

The trigger mechanisms can be related to one another as shown in Fig. 18. All systems begin in the box labeled "stability" and finish in the ovals "null mode" or "instability" when they fail. Most systems make the transition directly, but a few pass by the box labeled "ambushed transition." In this case, the initial rise in kinetic energy is caused by an oscillation provoked by a transition between two stable states, as discussed in Sec. IV E. During the oscillation, a null mode or instability appears which then causes the system to fail. During the course of failure, null modes can appear or disappear. The same figure also ranks the different trigger mechanisms by their stability. The lower they appear, the more unstable they are. Thus the upper region of the figure is labeled $\mathbf{vkv}>0$ and includes stability and ambushed transition, for the packing is stable in these states. The lower part of the figure is labeled $\mathbf{vkv}<0$ and contains the oval instability. The two parts of the figure are separated by a horizontal dotted line representing the condition $\mathbf{vkv}=0$ which is met in the oval null mode.

TABLE II. Number of systems that fail through the different trigger mechanisms for different numbers of particles.

	$N=16$	$N=32$	$N=64$
Ambushed	4	10	12
$\mathbf{vkv}=0$	14	1	0
Instability ($\mathbf{vkv}>-\mathbf{v\dot{c}F}$)	8	8	5
Total	26	19	17

F. Trigger in larger systems

So far we considered trigger mechanisms in small packings with 16 particles, where the influence of the boundary conditions is quite pronounced. In larger systems, the relative occurrence of the trigger mechanisms might be different. This section tackles this question and provides statistics of the trigger mechanisms as a function of system size.

In Table II the number of systems that fail through the different trigger mechanisms are listed for systems with $N=16$, 32, and 64 particles. First, the number of instabilities slightly decreases with increasing system size. This means that the system passes through one of the other trigger mechanisms before instability appears (see Fig. 18). Second we note that a lot of small systems with $N=16$ particles fail through the null-mode trigger, but only one system with 32 particles shows this trigger mechanism. No larger system was found to fail through the occurrence of a null mode. On the other hand, the more complex trigger ambushed transition becomes more frequent when the system size is increased. For $N=32$ particles systems, this is already the most common trigger of failure. An argument for this turnaround is that each contact has a smaller effect on the stiffness. Thus the stiffness will not directly jump to a negative value through a single contact status change. Instead, the stiffness will decrease by small steps and often arrive in the "soft" region, where deformations are large. Another argument for the rising number of ambushed transitions is the increase in vibrations. This increase has several origins. First we have more vibration modes, as their number linearly increases with system size. Second, the longer the wavelength of such a vibration, the less it is damped and the longest wavelength is comparable to the size of the system. Third we have much more contact changes in the same time interval, so the time for one vibration to be damped is much shorter before the next status change appears.

The striking number of null-mode triggers in the small systems is worth some closer examination. In Fig. 5 we showed that, occasionally, a granular assembly can form a square structure. This square structure has only circuits with four grains, which explains why the rotation movement is possible: in even circuits, all the grains can rotate in opposite direction at their points of contact. If there is an uneven circuit then at least one contact has to be sliding in order to allow for this movement. This is because in odd circuits there is at least one contact at which the grains have to move in the *same* direction. This is only possible if it is a sliding contact.

In Table III the number of circuits for systems with $N=16$ and 32 particles are compared. Because there is only

TABLE III. Average number of circuits per system for systems with $N=16$ and $N=32$ particles.

Circuit	$N=16$	$N=32$
3	1.58	5.37
4	3.62	8.58
5	1.65	4.58
6	0.15	1.11
7	0.12	0.42
8	0	0.16
9	0	0.05

one null-mode trigger for $N=32$, we average over all trigger mechanisms that can appear.

The average number of even circuits in $N=32$ particle systems is 9.85, slightly lower than the number of odd circuits 10.42. This is opposite to the $N=16$ particles systems, where the number of even circuits 3.77 is higher than the number of odd circuits 3.35. We argue that the main difference between these two systems is not the system size, but the tendency to form a square structure. While 4 by 4 ($N=16$) is innately square, $4\sqrt{2}$ by $4\sqrt{2}(N=32)$ is incompatible with a square structure. This preference also explains, at least partially, the high number of null-mode triggers in the $N=16$ particles systems.

On the other hand, 64 particles assemblies can form a square structure, but the probability of it being disrupted by "defects" due to polydispersity is much higher. Accordingly, we do not observe any null-mode failure for this system size. Therefore boundary effects seem to be very important in the $N=16$ particles assemblies.

A more thorough investigation of null-mode motions is shown in Table IV, where the number of null modes is listed as a function of system size, before, at, and after the time when the trigger appears. The result shows a clear tendency: the larger the system the less number of null modes decreases as the system increases. Before failure, there are already no more null modes for $N=32$, while at t_{trigger} we have to take systems with at least $N=64$ particles to get rid of them. During the failure, the number of null modes does not vanish for any of the system sizes, but the trend toward fewer null modes in large systems remains.

We furthermore tested if, in the smallest systems, the number of null modes depends on the wall friction. When we reran the $N=16$ simulations with friction at the walls we

TABLE IV. Average number of nontrivial null-mode movements per system for different system sizes at the times $t=t_{\mathrm{trigger}}-0.2$ (before), $t=t_{\mathrm{trigger}}$, and $t=t_{\mathrm{trigger}}+0.2$ (during the failure).

N	Nontrivial null-mode movements		
	Before	At t_{trigger}	During failure
16	0.19	0.69	0.62
32	0.00	0.11	0.32
64	0.00	0.00	0.21

found that failure is almost always accompanied by the appearance of a null mode. Therefore the observed null modes seem to be a proper feature of the failure process and not due to the absence of wall friction. However, those systems were not subjected to the lengthy process of a detailed analysis of the trigger mechanisms.

G. What drives failure?

We now discuss the kinetic energy in the $N=16$ particle packings.

1. Exponential rise of the kinetic energy

During failure, the kinetic energy rises exponentially; $E_{\mathrm{kin}} \propto e^{\beta t}$. To determine β, we took the points starting from the time when $E_{\mathrm{kin}}=10E_{\mathrm{kin}}(t_{\mathrm{trigger}})$ until $t=t_{\mathrm{trigger}}+1$ or the time when E_{kin} starts to decrease, whichever comes first. We call this "total fit" because it covers the whole exponential region. First we determined the exponent β directly from the kinetic energy observed in the simulations and we obtain $\beta=0.32\pm0.07\hat{f}/\hat{t}$ after averaging over all 26 seeds. Second, a prediction of β can be obtained from Eq. (28). This equation yields a slightly higher value of $\beta=0.33\pm0.09\hat{f}/\hat{t}$. Rattlers are one source of discrepancy, because they contribute to E_{kin} in the simulations, but are excluded from the theory. Furthermore, the neglect of damping contributions redounds to slightly higher values.

Toward the end of failure, the increase in kinetic energy is much more regular. Therefore, we performed a second "best fit" calculation of the exponent β in this region; we obtain $\beta=0.34\pm0.10\hat{f}/\hat{t}$, which is very close to the value found by fitting the whole curve. Hence, the mean exponent β is a robust feature of failure.

2. Sources of energy

The mechanism that drives failure can be uncovered by comparing the various terms in Eq. (28). There are three contributions to $\ddot{E}_{\mathrm{kin}}$ that can dominate: the force imbalance, the mechanical stiffness, or the geometric stiffness. These contributions are proportional to $\mathbf{vv}$, so they should be almost constant when divided by E_{kin}. The term $\mathbf{v}\dot{\mathbf{f}}_{\mathrm{ext}}$ is negligible in the exponential region, because it is proportional to $\mathbf{v}$, so its contribution to E_{kin} evolves like $|\mathbf{v}|/E_{\mathrm{kin}}\to0$. This term does have a very special role at the onset of failure, however. In all 26 cases we have examined, it is the main source of energy at t_{trigger}, but is then quickly replaced by the force imbalance. The damping, omitted from Eq. (28), cannot drive failure, since it always opposes motion.

The relative contributions to $\ddot{E}_{\mathrm{kin}}$ averaged over all assemblies are given in Table V. The two rows correspond to the two different methods of averaging discussed in the previous subsection: the first row covers the whole exponential region, whereas the second row applies to the latter part. The variance of each contribution is much larger in the first row than in the second, which is a consequence of the fluctuations in Figs. 10 and 14 at the onset of failure. On the contrary, the

TABLE V. Average theoretical exponential slope β and principal contributions to the second derivative of E_{kin} during failure. The average has been carried out over 26 systems. The upper values are obtained by fitting the whole exponential region (total fit) while the bottom values stem from a fit to 15 consecutive points of almost constant contributions (best fit). Note that $\mathbf{m\dot{v}} = \mathbf{f}_{\text{ext}} + \mathbf{cF}$ is the force imbalance.

	β	Contributions to $\ddot{E}_{\text{kin}}$ (in %)			
		$\mathbf{\dot{v}m\dot{v}}$	$\mathbf{vkv}$	$\mathbf{v\dot{c}F}$	Sum
Total fit	0.33 ± 0.09	93 ± 89	-25 ± 98	27 ± 19	95
Best fit	0.34 ± 0.10	72 ± 09	00 ± 18	25 ± 13	97

latter, best fit part of the curve is very regular. This is a general feature of all the simulations.

The table also shows that the force imbalance contributes the largest part to $\ddot{E}_{\text{kin}}$, followed by the contribution of the geometric stiffness. The mechanical stiffness contribution is small, on average. It can indeed, depending on the system, be either positive or negative, driving or opposing failure. Thus the two stiffnesses do not directly drive failure; instead, they generate the force imbalance at the beginning of failure. Recall that a negative stiffness drives the system away from its equilibrium position, the force imbalance will become larger the more the system departs from its initial configuration. This evolution will eventually come to an end when a new stable state is experienced. This can be seen most clearly in Fig. 10, where the exponential rise of the kinetic energy is broken at $t - t_{\text{trigger}} \approx 0.7$, and the mechanical stiffness begins to fluctuate wildly, presumably due to vibrations. This process is not related to the onset of failure, and we have therefore not investigated it in detail.

H. Failure staircase

In this paper, we define failure to occur at the first abrupt change in the strain. However, this event may be simply the first of a series. This possibility is suggested by the observation made at the end of the previous section: the system finds a new stable state when the exponential rise in kinetic energy is broken. The experiment could be continued until the second stable state collapses, leading to a third stable state, and so on. Finally the grains will form a monolayer and no further failure events are possible. Thus the strain as a function of time will be a staircase with the steps corresponding to the events studied in this paper. This is reminiscent of the devil's staircase observed in packings of perfectly rigid, frictionless grains [20].

In the small packings considered here, the number of steps in the staircase must be small, but in larger systems, there could be many more, and the size of the steps could become small. Strain-controlled simulations of rigid frictional particles [21] suggest there are many stable states that the system passes through as it deforms. If this were true, what is called failure in large systems must be characterized by something in addition to an instability: the next stable state must be far away, so that a large change in the strain

occurs. A satisfactory evaluation of this speculation is beyond the scope of this paper, for the appearance of failure depends on many factors: the preparation procedure, the boundary conditions (stress- or strain-controlled), the rate at which the stress or strain is modified (if not quasistatic), the stiffness of the particles, etc. We therefore leave this point open to further investigations.

VI. CONCLUSION

We have studied failure in numerical simulations of small granular assemblies composed of 16 particles subjected to a slowly increasing deviatoric stress under biaxial boundary conditions. This system size is small enough to allow for a detailed analysis of failure, but large enough to exhibit complex behavior. 26 different configurations were studied and we use stiffness matrix theory to understand the results.

We first studied the assemblies as the load was increased. As in previous works [22–24], we find a reduction in stiffness together with an increasing number of sliding contacts. The stiffness occasionally increases, but usually declines, always in a stepwise fashion, with sudden drops coinciding with contact status changes. These status changes are accompanied by damped oscillations.

Our initial expectation for the cause of failure was based on Ref. [9]: failure would be triggered by a contact status change that leads to a negative stiffness or a null mode. Negative stiffness means that an increment of force pushes the system away from its equilibrium and a null mode is a motion that does not change the contact forces at all. This expectation was to a large degree confirmed. Failure could always be associated with a contact status change that initiates the "trigger" of failure. Furthermore, 22 out of the 26 assemblies failed through a null mode or instability. The remaining four assemblies fail through a process that we call ambushed transition: the initial rise in kinetic energy is caused by oscillations provoked by a transition between two stable states. During these oscillations, a second status change occurs that leads to a null mode or to an instability, and thus to failure.

To assess the significance of ambushed transitions, one would have to study carefully the oscillations and their dependence on numerous parameters: the rate of loading, the stiffness of the particles, the damping, the size of the system, the boundary conditions, and dimensionality (two or three dimensions) all affect the vibrations and must be considered. At present, little has been done to answer the question of whether the vibrations in our ambushed transitions are a serious issue in real systems.

The intent of this paper is to show that the stiffness matrix can describe the quasistatic behavior of granular material on the way to failure. Our results show that in the limit of sufficiently stiff particles, inertia and dissipation become irrelevant. Furthermore the present study shows that the stiffness matrix can explain to a large extent the mechanisms leading to the collapse of granular assemblies.

In addition to the trigger of failure, we also examined the process of failure itself by determining the various contributions to the kinetic energy. Before failure, energy is injected

by the external load and stored as potential energy in the contacts by the mechanical stiffness. Just at failure, the mechanical stiffness is reduced and can no longer compensate for the energy injected by the load, and the kinetic energy begins to rise. Shortly thereafter, however, the dominate source of energy is force disequilibrium.

The kinetic energy always rises exponentially during failure. Reference [9] expected that this would be so only when failure was triggered by an instability. For a null mode, the energy was expected to rise algebraically. A detailed analysis shows that the geometric stiffness, which has not been anticipated by Ref. [9], then becomes significant at failure, leading to the exponential rise of the energy. In agreement with Ref. [7], we find that the geometric stiffness is always destabilizing. Hence failure involves always an exponentially rising kinetic energy.

What will happen in large systems? It will certainly become more difficult to identify the cause of failure: while in small systems the contact status changes can be well separated in time and thus the effect of each one can be ascertained, in large systems the changes will be more frequent, and also each one has a smaller effect. Thus the steps with which the stiffness declines will decrease with system size, and finally, the stiffness can be approximated by a continuous function. This means that the mechanical stiffness cannot suddenly become negative, or zero, as in many examples in this paper. We expect therefore that it will decline until it is canceled out by the geometric stiffness, and failure will occur. Just before this happens, however, the packing will be very soft, and ambushed transitions will occur frequently. Our observations of larger systems containing 64 particles confirm these trends. Furthermore we anticipate that compound status changes will become more frequent in large systems. Therefore they might be more often involved in the occurrence of failure in large systems.

We did not find any precursors to failure in small systems. This might be due to the limited number of possible contact status changes and the large resulting change in stiffness. However, precursors might be frequently encountered in large systems. We suspect that they look like failure itself but limited to localized regions. Then, little by little, the mean size of these regions may become bigger and bigger, until they merge and spread across the entire system. Other investigations are in favor of this speculation, as they show that criticality (i.e., instability) is restricted to regions where shear bands with unique characteristics develop [25,26].

ACKNOWLEDGMENTS

APPENDIX A: INVERSION OF THE STIFFNESS MATRIX

As discussed in Sec. III D 3, the stiffness matrix is always singular. Nevertheless, it is possible to construct a matrix that acts as its inverse. To do so, we decompose the matrix into a diagonal matrix $\mathbf{s}$ and two orthonormal matrices $\mathbf{u}$ and $\mathbf{w}$,

$$\mathbf{u}\mathbf{s}\mathbf{w}^T = \mathbf{k}. \tag{A1}$$

This reduction is called singular value decomposition and is always possible, with $\mathbf{s}$ containing the (non-negative) real singular values. Note that $\mathbf{k}$ is not symmetric, so it can in general not be diagonalized over $\mathfrak{R}$ (some of the eigenvalues would be complex). To define a matrix that acts as an inverse of $\mathbf{k}$, we first define

$$\widetilde{s}_{ij} := \begin{cases} 1/s_{ii} & \text{if } i=j \text{ and } s_{ii} \neq 0, \\ 0 & \text{otherwise}. \end{cases} \tag{A2}$$

Then the "inverse" of the stiffness matrix is defined as

$$\widetilde{\mathbf{k}} := \mathbf{w}\widetilde{\mathbf{s}}\mathbf{u}^T. \tag{A3}$$

Note that, by definition, the kernel dimensions of $\mathbf{k}$ and of $\widetilde{\mathbf{k}}$ are identical.

APPENDIX B: THE GEOMETRIC STIFFNESS

We will now show an argument why the geometric stiffness contribution $\mathbf{v}\dot{\mathbf{c}}\mathbf{F}$ constitutes an instability for circular grains. We start writing the configuration matrix $c_{i\alpha}$ [10] for contact α of grain i:

$$c_{i\alpha} = \begin{pmatrix} \vec{n}_\alpha & \vec{t}_\alpha \\ 0 & 1 \end{pmatrix}. \tag{B1}$$

Note that we are in two dimensions and the third line denotes the rotational part of the mapping from the contact (force) space to the particle (force) space. The derivative of $c_{i\alpha}$ quantifies the change in contact direction $\vec{n}_\alpha$. We will limit the discussion to only one contact, but the generalization is straightforward. Introducing the particle center distance $\vec{X}_{ij} = \vec{x}_i - \vec{x}_j$, its length $X_{ij} = |\vec{X}_{ij}|$, and its derivative $\vec{V}_{ij} = \vec{v}_i - \vec{v}_j$, we get

$$\dot{\vec{n}}_\alpha = \frac{d}{dt}\frac{\vec{X}_{ij}}{X_{ij}} = \frac{\vec{V}_{ij}}{X_{ij}} - \frac{\vec{n}_\alpha(\vec{n}_\alpha \cdot \vec{V}_{ij})}{X_{ij}} = \frac{\vec{t}_\alpha(\vec{t}_\alpha \cdot \vec{V}_{ij})}{X_{ij}}. \tag{B2}$$

$\dot{\vec{t}}_\alpha$ is then obtained from the relation

$$\dot{\vec{t}}_\alpha = \vec{e}_z \times \dot{\vec{n}}_\alpha = -\vec{n}_\alpha\frac{(\vec{t}_\alpha \cdot \vec{V}_{ij})}{X_{ij}}, \tag{B3}$$

where $\vec{e}_z$ is the unit vector along z and orthogonal to both $\vec{n}$ and $\vec{t}$. The quantity in brackets is the tangential velocity V^t_{ij}. The derivative of $c_{i\alpha}$ is linear in this quantity,

$$\dot{c}_{i\alpha} = \frac{V^t_{ij}}{X_{ij}}\begin{pmatrix} \vec{t}_\alpha & -\vec{n}_\alpha \\ 0 & 0 \end{pmatrix}. \tag{B4}$$

The contribution to the geometric stiffness of particle i at contact α is

$$\mathbf{v}_i^T\dot{\mathbf{c}}_{i\alpha}\mathbf{F}_\alpha = \frac{V^t_{ij}}{X_{ij}}(v_i^t F_\alpha^n - v_i^n F_\alpha^t). \tag{B5}$$

Now we include the contribution from particle j. Noting that $c_{j\alpha} = -c_{i\alpha}$ and defining $\widetilde{\mathbf{v}} := \mathbf{v_i} + \mathbf{v_j}$, we get

$$\tilde{\mathbf{v}}^T \dot{\mathbf{c}}_\alpha \mathbf{F}_\alpha = \frac{V_{ij}^t}{X_{ij}}(V_{ij}^t F_\alpha^n - V_{ij}^n F_\alpha^t). \tag{B6}$$

X_{ij} and F_α^n are always positive, the other quantities can be either positive or negative. Thus the second term can be either negative or positive and averaging over a large number of contacts leads to many cancellations. On the other hand, the first term is always positive. Hence $\mathbf{v}\dot{\mathbf{c}}\mathbf{F} > 0$ for assemblies of circular grains.

For stiff circular grains, the geometric stiffness is negligible in comparison to the mechanical part. The first is proportional to the average contact force, whereas the second depends on the contact stiffness. A rough estimation for their ratio is

$$\frac{\mathbf{v}^T \dot{\mathbf{c}} \mathbf{F}}{\mathbf{v}^T \mathbf{k} \mathbf{v}} \approx \frac{v \frac{v}{d} F}{v^2 k_n} \approx \frac{\frac{1}{d}\left(f_{\text{ext}} \frac{d}{L}\right)}{k_n} = \frac{f_{\text{ext}}}{k_n L} \approx 10^{-3}. \tag{B7}$$

Here, $d = 2r$ is the average grain diameter and $L \approx 4d$ is the length of the simulation box. The average contact force is denoted by F. This equation holds when there are no sliding contacts. The ratio can become significantly larger when their number increases. At failure, the geometric stiffness $\mathbf{v}\dot{\mathbf{c}}\mathbf{F}$ can even surpass the mechanical contribution.

APPENDIX C: CORRECTIONS TO c

Calculating the force balance in Eq. (27) or Eq. (28) with the **c** matrix, given for one contact in Eq. (B1), leads to a large force imbalance even when the simulation is quasistatic. This is because the configuration matrix $c_{i\alpha}$ given above is an approximation and the entries in the last line have to be corrected for the particle overlap. When we take it into account, we get for the second entry

$$1 - \frac{D_n}{r_i + r_j} = \frac{X_{ij}}{r_i + r_j}. \tag{C1}$$

The overlap distance D_n and the particle radii r_i, r_j had been introduced in Eq. (2). Taking the derivative of Eq. (C1), the correction to Eq. (B4) is

$$\dot{c}_{i\alpha} = \frac{V_{ij}^t}{X_{ij}} \begin{pmatrix} \tilde{t}_\alpha & -\vec{n}_\alpha \\ 0 & \dfrac{X_{ij}}{V_{ij}^t} \dfrac{V_{ij}^n}{r_i + r_j} \end{pmatrix}. \tag{C2}$$

It turns out that this correction is not crucial for the value of $\mathbf{v}\dot{\mathbf{c}}\mathbf{F}$ because its contribution is roughly 5%.

APPENDIX D: NULL MODES

In Sec. III D 1 we mentioned that a vanishing mechanical stiffness associated with the occurrence of a null mode can trigger the onset of failure. Here, we will present a very simplified model that gives some insight into its contribution to the kinetic energy. The assumption $\mathbf{kv} = 0$ means that larger external forces will not be balanced by the contact forces anymore. Then, the imbalance leads to a change in velocity of the particles induced by the change in the external forces [see Eq. (15)]:

$$m\ddot{v} = \dot{f}_{\text{ext}}. \tag{D1}$$

Here, we consider the mass of the granular assembly and the external force acting on it to be scalar quantities because the latter will set the forces acting on the particles. Presuming that the right side is constant, integrating twice leads to

$$mv = \frac{1}{2}\dot{f}_{\text{ext}}t^2 + m\dot{v}(t_0)t + mv_0. \tag{D2}$$

Just before the null mode occurs, $\dot{v}$ will be small, so we can neglect the contribution of the second term. With this simplification the kinetic energy writes

$$E_{\text{kin}} = \frac{1}{2}mv^2 = \frac{1}{8}t^4\frac{\dot{f}_{\text{ext}}^2}{m} + \frac{1}{2}t^2\dot{f}_{\text{ext}}v_0 + E_{\text{kin},0}. \tag{D3}$$

Please note that v is proportional to $\dot{f}_{\text{ext}}$, so $E_{\text{kin}} \propto \dot{f}_{\text{ext}}^2 + \mathcal{O}(\dot{f}_{\text{ext}})$. We checked this time dependence in one simulation and we found the scaling with $\dot{f}_{\text{ext}}$ and m predicted in Eq. (D3).

[1] A. Aydin, R. I. Borja, and P. Eichhubl, J. Struct. Geol. **28**, 83 (2006).

[2] P. V. Lade, Int. J. Solids Struct. **39**, 3337 (2002).

[3] A. J. Liu and S. Nagel, Nature (London) **396**, 21 (1998).

[4] C. S. O'Hern, S. A. Langer, A. J. Liu, and S. R. Nagel, Phys. Rev. Lett. **88**, 075507 (2002).

[5] K. Bagi, Granul. Matter **9**, 109 (2006).

[6] M. R. Kuhn and C. S. Chang, Int. J. Solids Struct. **43**, 6026 (2006).

[7] M. R. Kuhn, in *Powders and Grains 2005*, edited by R. García-Rojo *et al.* (Leiden, Balkema, 2005), pp. 115–122.

[8] K. Kaneko *et al.*, Int. J. Solids Struct. **40**, 4043 (2003).

[9] S. McNamara, R. Garcìa-Rojo, and H. Herrmann, Phys. Rev. E **72**, 021304 (2005).

[10] S. C. McNamara and H. J. Herrmann, Phys. Rev. E **74**, 061303 (2006).

[11] P. A. Cundall and O. D. L. Strack, Geotechnique **29**, 47 (1979).

[12] C. F. Moukarzel, Granul. Matter **3**, 41 (2001).

[13] I. Agnolin and J.-N. Roux, Phys. Rev. E **76**, 061302 (2007).

[14] J.-N. Roux, Phys. Rev. E **61**, 6802 (2000).

[15] C. F. Moukarzel, Phys. Rev. Lett. **81**, 1634 (1998).

[16] E. Somfai, M. van Hecke, W. G. Ellenbroek, K. Shundyak, and W. van Saarloos, Phys. Rev. E **75**, 020301(R) (2007).

[17] A. Kasahara and H. Nakanishi, Phys. Rev. E **70**, 051309 (2004).

[18] S. McNamara, R. Garcìa-Rojo, and H. J. Herrmann, in *Powders and Grains 2005*, edited by R. García-Rojo *et al.* (Leiden,

Balkema, 2005), pp. 295–299.

[19] R. Garcìa-Rojo, S. McNamara, A. A. Peña, and H. J. Herrmann, in *Powders and Grains 2005*, edited by R. García-Rojo *et al.* (Leiden, Balkema, 2005), pp. 705–708.

[20] G. Combe and J.-N. Roux, Phys. Rev. Lett. **85**, 3628 (2000).

[21] J.-N. Roux and G. Combe, C. R. Phys. **3**, 131 (2002).

[22] J.-N. Roux, in *Powders and Grains 2005*, edited by R. García-Rojo *et al.* (Leiden, Balkema, 2005), pp. 261–265.

[23] F. Alonso-Marroquín, S. Luding, H. J. Herrmann, and I. Vard-

oulakis, Phys. Rev. E **71**, 051304 (2005).

[24] S. Luding and H. J. Herrmann, in *Zur Beschreibung komplexen Materialverhaltens, Institut für Mechanik, Stuttgart* (S. Diebels, Stuttgart, 2001), pp. 121–134.

[25] S. Fazekas, J. Török, and J. Kertész, Phys. Rev. E **75**, 011302 (2007).

[26] L. Rothenburg and N. P. Kruyt, Int. J. Solids Struct. **41**, 5763 (2004).